Ceramics International 48 (2022) 12721–12728

Contents lists available at ScienceDirect

Ceramics International

journal homepage: www.elsevier.com/locate/ceramint

Additive manufacturing of borosilicate glass via stereolithography

Omena Okpowe [a], Vadym Drozd [a,b], Oscar Ares-Muzio [c], Nezih Pala [c], Chunlei Wang [a,b,*]

[a] Mechanical and Materials Engineering Department, Florida International University, United States
[b] Center for Study of Matter at Extreme Conditions, Florida International University, United States
[c] Electrical and Computer Engineering Department, Florida International University, United States

ARTICLE INFO

Keywords:
Stereolithography
Borosilicate
Cerium doping
Calcination
Densification
Luminescence

ABSTRACT

Recent surge in additive manufacturing efforts demonstrate stereolithography as a promising technique for fabricating glass materials due to the high speed and scalability of the process. However, little efforts have been devoted to manufacture borosilicate glass by the stereolithographic process. One of the challenges is that its relatively low softening temperatures could interfere with the thermal post-printing process and introduce poor fidelity and structure instability. Here, we report on the first demonstration of stereolithographic manufacturing of cerium-doped (Ce-doped) (<10%) and undoped borosilicate glass which was enabled by a multi-step post thermal processing. The optical properties of the printed glass depend on thermal processing parameters (temperature, time, and environment) and can be readily tuned and optimized for a wide range of applications. The printed amorphous glass shows good structural stability with band gap of 3 eV, Urbach energy of 0.75 eV and refractive index of 2.14 for 8% Ce-doped glass, respectively. These results indicate Ce-doped glass fabricated by stereolithography is suitable for scintillator applications and that additive manufacturing could be promising for borosilicate glass fabrication.

1. Introduction

Borosilicate ($B–SiO_2$) glass consists of SiO_2 and B_2O_3 as network formers and alkali oxide modifiers respectively. Its excellent optical properties such as transparency and tunable refractive index, chemical resistance, low thermal expansivity and tunable chemical composition make it useful for a wide range of applications such as luminescence [1,2]; optical lenses [3]; electrochromism [4], lab ware, medical implants, waste immobilization [5], and other microelectromechanical systems (MEMS). In addition, the high thermal neutron cross-section of boron and high luminescence efficiency of Cerium (Ce) makes Ce-doped borosilicate glass a perfect scintillator material for radiation detection [6–9]. The optical properties of glass fabricated by conventional melt-quenching or high temperature densification approaches depend on the glass fabrication method, precursors and processing conditions for incorporation of Ce into the $B–SiO_2$ matrix [1]. However, the conventional glass fabrication based on melt-quenching resorts to relatively high temperatures (>1000 °C) for melting and also needs reduced environment to ensure the dopant state during the melt and cooling process.

Recently, additive manufacturing of $B–SiO_2$ ceramics has been demonstrated by various 3D printing techniques such as: selective laser melting (SLM) [10], direct laser sintering (DLS) [11] and fused deposition modeling (FDM). Both SLM and DLS are powder bed fusion techniques where powders are consolidated either by melting or by densification using a high-power density heat source such as a CO_2 laser or electron beams. These glasses were shown to exhibit high porosity and low optical transparency. FDM utilizes a CO_2 laser heat source to generate molten glass from glass filaments [12,13]. Other than its low resolution, the other key challenge with FDM for $B–SiO_2$ glass formation is the bubble formation resulting from the printing process, which has been shown to be resolvable by carrying out systematic post-annealing [12,13]. Other glass additive manufacturing approaches, such as material extrusion and stop flow lithography [14] have also been reported for SiO_2 glass fabrication with issues of relatively rough surface finishing and difficulty to form complex 3D structure, respectively. More recently, the exploration of sludge based additive manufacturing accompanied by a subsequent heat treatment step at relatively low temperatures have been shown to be a preferable route for glass fabrication as they helped overcome the challenges of melt-quenching [15–18].

The sludge-based technique typically entails either direct ink writing (DIW), digital light processing (DLP) or stereolithography (SLA) and

* Corresponding author. Mechanical and Materials Engineering Department, Florida International University, United States.
E-mail address: wangc@fiu.edu (C. Wang).

https://doi.org/10.1016/j.ceramint.2022.01.141
Received 14 October 2021; Received in revised form 7 January 2022; Accepted 13 January 2022
Available online 18 January 2022

allows for a room temperature printing after which the thermal processing can be carried out usually below the softening temperature of the ceramic material. The DIW technique was first patented for additive manufacturing of ceramics in 2000 by Cesarano et al. [19]. It had been used for 3D printing a wide range of materials such as photonic crystals [20,21] and energy devices [22] until its recent success in 2017 with glass materials [17]. In terms of DIW, the rheological properties of the sludge are tuned in such a way that in the presence of a shear force the viscous liquid flows and thins to maximize the z-resolution of the eventual prints and then stops when the force is removed however, the process is subjected to a relatively long (110 h) drying, calcination and the densification process. SLA, a vat photopolymerization technique, invented by Chucks Hall in 1986 on the other hand, typically entails curing a liquid photosensitive pre-polymer resin mixture by an irradiation light source (most commonly UV) [23]. The latter induces a chemical reaction by first attacking the photoinitiator, which in turn reacts with the monomers and oligomers in the mix resulting in a highly cross-linked polymer network. In terms of ceramics printing by SLA, a homogeneous photocurable sludge based on mixing and dispersing of a pre-polymer photosensitive resin mixture with ceramic filler particles can be formed with the aid of surfactants or additives. Recently Rapp and coworkers at KIT have successfully synthesized high-resolution undoped and amorphous pure silica glass by SLA using 40 nm fumed silica particles and high molecular weight acrylate-based resin in a multi-step calcination and densification process (1300 °C) [15,24]. By immersing the brown body in solutions of alcohol and metal salts, they were able to obtain colored glasses with different optical transmission characteristics. Following the pioneer work of KIT there are several other groups developing SLA based process for transparent silica glass manufacturing with noticeable progress towards photovoltaic applications and general process improvement [16]. All these works have demonstrated that SLA is a promising approach for printing fine details and complex geometric structures since the resolution depends on the dimensions of the laser beam. However, several challenges of SLA based glass fabrication have to be further addressed. The rheological properties and optical properties of the sludge and the eventual shrinkage in the final glass product are all dependent on the sludge compositions. The viscosity of commercially available resins is close to 3000 mPas. The typical volumetric composition of sludge (ceramics in the resin) ranges from 30 vol% (low viscosity) to 60 vol % (high viscosity). Higher viscosities could help to maintain the structure stability with lower shrinkage of final products but with the trade-off of light scattering and printability. In addition, refractive index matching of the polymer resin and the ceramic particles is key for higher degree of structure fidelity [25]. Moreover, the relatively low softening temperature (T_s) for B–SiO_2 (~711 °C) makes the thermal treatment step cumbersome partially because of an overlap of the calcination and densification thermal processing regions.

In the present work, we demonstrate, 3D-printed B–SiO_2 glass fabricated via stereolithography with comparable optical properties to commercial B–SiO_2 glass, irrespective of their low softening temperatures. The processing parameters of densification and calcination were optimized to achieve structure stability of the resulting undoped and Ce-doped B–SiO_2 glass. Optical parameters including the optical band gap, Urbach energy and refractive index were deduced from the optical absorption spectra with comparable quality to doped glasses fabricated by conventional melt quench method.

2. Experimental

The glasses were fabricated by first mixing B–SiO_2 7070 (Corning Inc.) with acrylate-based pre-polymer resin-mix comprising hydroxyethyl methacrylate (HEMA) (Sigma Aldrich Inc.), trimethylolpropane ethoxylate triacrylate (Sigma Aldrich Inc.), hydroquinone (Sigma Aldrich Inc.), Tinuvin 384-2 (Ribelin Inc.) and 0.5 wt% of phenylbis (2,4,6-trimethylbenzoyl) phosphine oxide (Sigma Aldrich Inc.) in the ratio of 100:50:7:6:7 by weight, respectively or Formlabs 1+ clear resin (Formlabs Inc.). Some properties of the B–SiO_2 powder, its scanning electron morphology as well as BET surface area morphology and porosity are indicated in Table S1, Fig. S1(a) and Fig. S1(b) respectively. The composition of the sludge was 40 vol % of the B–SiO_2 particles, printed and then calcined before densification. For the cerium doped glass, cerium (III) acetate sesquihydrate (Fisher Scientific Inc.) was introduced into the sludge at mole ratios varying from 0.1 to 1 mol % with respect to the B–SiO_2. The individual components of the liquid sludge were mixed before the dispersion using a hotplate stirrer. The resulting sludge was then degassed under vacuum before 3D printing. Detailed description of the prepared samples is summarized in Table 1. For sample nomenclature, the first 3 digits indicate the number of calcination steps, middle digits indicate the maximum calcination temperature and last digits indicate the densification time for undoped samples. Additional post-subscripts indicate either a non-vacuum environment (ambient air) or the volume composition of B–SiO_2 in the sludge. Doped samples are indicated by the chemical symbol of the dopant used (e.g. Ce for Cerium-doped). Table 2 lists the samples following the same nomenclature except that the dopant concentrations for doped samples are indicated as the last two digits in place of the densification times. The green body is the 3D-printed body whereas the calcined body is the sample obtained when the green body is subjected to thermal treatment in air to eliminate polymeric components and then the densified body is obtained when the calcined body is subjected to further processing to eliminate porosities and increase density of the sample.

The 3D printing process was carried out using a Formlabs 1+ 3D printer ($\lambda = 405$ nm) with an XY-resolution of 300 μm based on custom CAD-designs on a Solid Works software. The lateral and Z-direction resolutions were set to 0.2 mm for all printing. The obtained green body was then detached from their support structures, rinsed in ethanol, post cured using a 15-Watt 365 nm Blak-Ray XX-15BLB UV bench lamp for about 10min before being carefully moved to a furnace for thermal processing. The thermal processing was carried out at calcination and densification temperatures based on Table 1, which described specifics and fabrication conditions of samples. An Isotemp Muffle Furnace (Fisher Scientific) with a rotary pump mounted on it was utilized for these processes.

Scanning Electron Microscopy (SEM), JEOL JSM-6330F field emission SEM-EDS (Tokyo, Japan), was employed to investigate the morphology of the resulting body at various steps of the fabrication process. Energy Dispersive X-ray Spectroscopy (EDS) was used to ascertain the elemental composition of the resulting products. The presence and degree of devitrification of fabricated products were studied by X-ray diffraction (XRD) technique using a Siemens D-5000 X-ray diffractometer (Munich, Germany) which utilizes a copper K_α X-ray source of wavelength 1.54178 Å. The scan rate used was 0.1°/min while step size was 0.02°.

The surface area and porosities were determined by nitrogen adsorption/desorption isotherms at 77 K using a Tri-Star II Micromeritics and calculated by Brunauer–Emmett–Teller (BET) measurement. Prior to the measurements, all of the samples were degassed at 373 K for 24 h and finally outgassed to 10^{-3} Torr. The Differential Scanning Calorimetry (DSC) and Thermogravimetric Analysis (TGA) experiments were both carried out using a Simultaneous DSC-TGA (SDT) Q600 instrument. The light transmittance and absorption at different wavelengths of the final densified body are investigated using a Solar Cell Spectral response measurement system (PV measurements, Inc (Model QEX10)) whereas the luminescence properties are investigated by a Shimadzu RF-1501 spectrofluorophotometer.

3. Results and discussion

The schematic for the entire fabrication process is illustrated in Fig. 1. First, the Cerium acetate, B–SiO_2 particles and resin mixture are

Table 1
Summary of synthesis parameters of 3D printed B–SiO_2 glass samples.

Sample	Sludge B–SiO_2 vol (%)	Calcination						Densification		
		T_{c1} (°C)	t_{c1}(h)	T_{c2} (°C)	t_{c2}(h)	T_{c3} (°C)	t_{c3}(h)	T_d (°C)	t_d(h)	Environment
$(1SC-575-10)_{40}$	40	–	–	–	–	575	10	700	10	Vacuum
$(3SC-575-05)_{40}$	40	180	5	360	5	575	5	700	5	Vacuum
$(3SC-500-10)_{40}$	40	180	5	360	5	500	5	700	10	Vacuum
$(3SC-500-02)_{40}$	40	180	5	360	5	500	5	700	2	Vacuum
$(3SC-600-05)_{40}$	40	180	5	360	5	600	5	700	5	Vacuum
$(3SC-575-10)_{40}$	40	180	5	360	5	575	5	700	10	Vacuum
$(3SC-575-10)_{40+air}$	40	180	5	360	5	575	5	700	10	Air
$(3SC-575-10)_{20}$	20	180	5	360	5	575	5	700	10	Vacuum
$(3SC-575-10)_{60}$	60	180	5	360	5	575	5	700	10	Vacuum

Table 2
Summary of synthesis parameters of 3D printed B–SiO_2 glasses with different amount of Ce dopant.

Sample	Sludge B–SiO_2 vol (%)	Calcination						Dopant conc. (mol %)	Sample thickness (mm)
		T_{c1} (°C)	t_{c1}(h)	T_{c2} (°C)	t_{c2}(h)	T_{c3} (°C)	t_{c3}(h)		
Ce:3SC-575-02	40	180	5	360	5	575	5	2	1.73
Ce:3SC-575-04	40	180	5	360	5	575	5	4	1.15
Ce:3SC-575-06	40	180	5	360	5	575	5	6	1.39
Ce:3SC-575-08	40	180	5	360	5	575	5	8	2.06
Ce:3SC-575-10	40	180	5	360	5	575	5	10	2.16

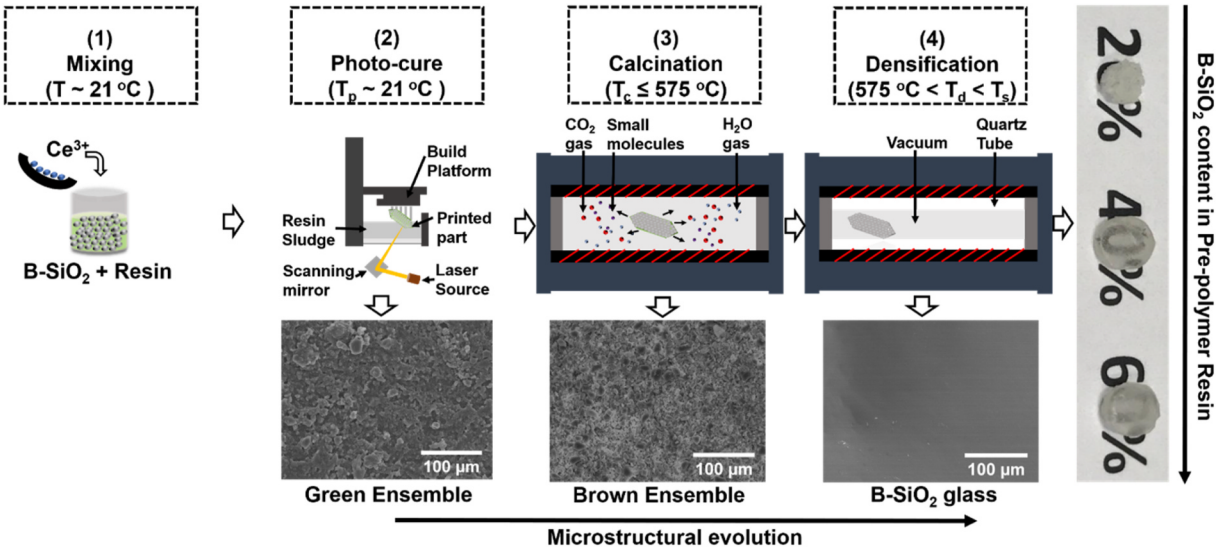

Fig. 1. Schematic illustration of the key steps in the fabrication of 3D borosilicate glass bodies. T_p, T_c, T_d and T_s represent printing, calcination, densification and softening temperatures, respectively. Step (1): Mixing step (and incorporation of Ce dopant); Step (2): Printing and photocuring process of the sludge using the SLA 3D-Printer; Step (3): Calcination process of the green body in the furnace; Step (4): Densification process of the calcined B–SiO_2 within a vacuumed quartz tube in the furnace. Bottom images show the scanning electron micrographs of the green body (left); calcined body (middle); and the densified body (right). Right images indicate the glass samples with increasing (indicated) ceramic particle loading (Samples $(3SC-575-10)_{20}$; $(3SC-575-10)_{40}$; $(3SC-575-10)_{60}$). (For interpretation of the references to color in this figure legend, the reader is referred to the Web version of this article.)

mixed at room temperature after which they are printed and cured with the aid of the SLA printer, calcined and densified. Fig. S1(a) shows the scanning electron microscopy image of the as-received B–SiO ceramics powder and this expectedly exhibits particle dimensions <40 µm. From Fig. S1(b) it is evident from the BET measurement that there is a complete absence of porosity in B–SiO_2 sample unlike compared to commercial SBA-15 whose pore size and distribution is well established. We also estimate the surface area to be 282.01 m^2/g as presented in Table S1. Fig. S2 shows a Computer Aided designed structure and some printed structures before calcination. The exemplary resulting densified glass samples for different particle loading in the liquid sludge body used for printing are shown on the right-hand side of Fig. 1. For a 20% particle loading by volume, there is an expectedly observed distorted opaque structure signifying a too low loading. However, the optical clarity increases with increasing loading due to decreasing degree of porosity. SEM images of the printed, calcined, and densified samples are also shown in Fig. 1. There is a high degree of porosity after calcination, which is as a result of the complete elimination of the polymeric component of the printed body, but this porosity is absent at the end of the densification process.

For the thermal analysis of B–SiO_2 powder (control sample) and B–SiO_2-resin green body sample ($(3SC-575-10)_{20}$) investigated and shown in Fig. 2(a), the temperature heat flow profile alongside a corresponding decomposition of the green body as a function of temperature for a ramping of 10 °C/min is presented. The DSC plot shows the heat flow versus temperature behavior of the borosilicate particles

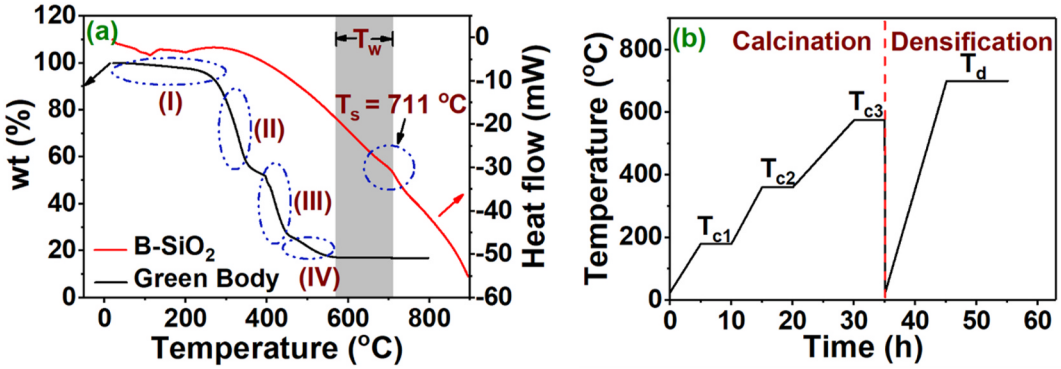

Fig. 2. (a) DSC and TGA curves for B–SiO_2 powder and B–SiO_2-resin green body respectively for temperature ramping of 10 °C/min in air. The regions (I)-(IV) indicate elimination of solvents, depolymerization, side chain reactions and elimination of residual polymer network component, respectively. (b) Thermal protocol for the calcination and densification of the B–SiO_2 body. The temperature-time conditions, T_{c1}, T_{c2} and T_{c3} indicate conditions allowing for gradual and steady reactions for the regions (I) – (IV). T_{c1} corresponds to the mid-temperature of region I in Fig. 2a; T_{c2} corresponds to the temperature boundary between region II and III in Fig. 2a. T_{c3} is the degradation-offset temperature established in Fig. 2a. T_d is densification temperature. (For interpretation of the references to color in this figure legend, the reader is referred to the Web version of this article.)

where the softening temperature for the B–SiO_2 glass is observed to be at 711 °C with an exothermic peak. For the degradation of $(3SC\text{-}575\text{-}10)_{20}$, initially there is a super-slow process (region I) where weight is constant up to 250 °C implying complete curing and absence of residual monomers or oligomers within the body structure. Beyond this temperature, there exist three, relatively faster, main stages of decomposition which may be ascribed to depolymerization with elimination of chain-end monomers (region II), side-chain reactions involving chain scissions (region III), and carbon skeleton degradation (region IV), respectively. Overall, there is an ~80% weight loss for the TGA analysis of sample $(3SC\text{-}575\text{-}10)_{20}$ which indicates a complete elimination of the polymeric component corresponding to a prepolymer resin sludge – ceramic initial loading ratio of 4:1 for the green body. To optimize the calcination process, sufficient times of 5 h each are given at selected temperatures within these three regions (T_{c1} = 180 °C, T_{c2} = 360 °C and T_{c3} = 575 °C) to allow for optimized calcination and negligible pulverization of the 3D printed structures resulting in the thermal protocol shown in the calcination stage of Fig. 2(b). The temperature range between the degradation offset temperature (575 °C) and the softening temperature of the B–SiO_2 (T_s = 711 °C) implies that there is a smaller window (T_w = 136 °C) for both calcination and densification for B–SiO_2 compared to other ceramic materials such as SiO_2 where this window is much wider (~5.3T_w) [15,17]. Fig. 2(b) gives the optimized thermal protocol used for the entire thermal processing based on the TGA behavior of the green body. The calcination region is where mostly the polymeric component is eliminated in the form of carbon (IV) oxide, steam, and other small molecules. Temperature-time condition, T_{c1}, corresponds to the mid-temperature of region I (in Fig. 2(a)), whereas the temperature-time condition T_{c2} corresponds to the temperature boundary between region II and III (in Fig. 2(a)). Temperature-time condition T_{c3} is the degradation-offset temperature established (in Fig. 2(a)) and the relatively slower ramp temperature between T_{c2} and T_{c3} was utilized because there is a higher tendency for pulverization at these temperature regions. An optimum temperature for densification (T_d = 700 °C ~ 98.5% T_s) was established and the densification was carried out for a sufficient time of 10 h as observed in Fig. 2(b) (temperature-time condition T_d).

The optical transparency property is key for glasses in general hence we investigated the optical transmittance property of the fabricated glass as a function of the particle loadings in the resin sludge. Under the same temperature, time and environmental conditions, we observed that Samples $(3SC\text{-}575\text{-}10)_{40}$ and $(3SC\text{-}575\text{-}10)_{60}$ with ceramic particle loadings of 40% and 60% yielded more transparent samples with better fidelity and we ascribe this to the fact that the densification conditions used reduced the porosities much without causing any devitrification whereas sample $(3SC\text{-}575\text{-}10)_{20}$ exhibited the least optical transparency as there was remnant porosity within its structure after densification. Its transmittance was only about 45% that of the $(3SC\text{-}575\text{-}10)_{40}$ sample. Fig. 3(a) however showed a better transmittance for a 40% loading compared to that for 60%, therefore most part of this work was carried out using a 40% loading. Apparently, there is a sintering temperature limit beyond which softening will occur (711 °C) altering the printed shape or causing devitrification. However, we presume that the use of finer and more homogenous ceramic precursor particles, appropriate sintering aids, extended sintering times or improved vacuum conditions could further improve the overall transmittance of the samples for desired applications.

Fig. 3(b) shows XRD patterns collected on the samples densified under ambient pressures and under vacuum using similar heat treatment protocols. Crystalline peaks observed at 27.6°, 42° and 51° can be ascribed to the formation of hexagonal quartz crystals with lattice parameters of a = 4.9127 Å and c = 5.4045 Å (space group $P3_221$) which are evidence of the devitrification [26]. Under vacuum densification, the sample remained amorphous with just the typical halo for amorphous materials observed, thus confirming the absence of devitrification as no crystalline peaks were observed. Fig. 3(c) shows the XRD results observed after densification in vacuum for different heat treatment protocol shown in Table 1. There are no observed continuous or discrete sharp devitrification peaks irrespective of the route taken; however, slight shifts in the amorphous halo peaks and magnitude are observable and these may be ascribed to varying degree of amorphousness as a result of the various thermal protocols [27]. The amorphous halo peaks for B–SiO_2 glass are typically observed at 26°. For the case of this work, the temperature of calcination has a negligible effect on the amorphous peak positions as observed when comparing samples $(1SC\text{-}575\text{-}10)_{40}$ to $(3SC\text{-}500\text{-}10)_{40}$ and $(3SC\text{-}575\text{-}05)_{40}$ to $(3SC\text{-}600\text{-}05)_{40}$; however, larger densification times (t_d) result in a more leftward deviation of the halo peak from this typical value (26°). We attribute this deviation to a gradual reorganization of the silicon oxide continuous random network towards the formation of a random close packed semi-phase leaving behind an amorphous halo rich in boron oxide.

Fig. 4(a) shows the EDS spectrum of the B–SiO_2 structure modified by Ce^{3+} ions with concentration 8 mol%. The 0.883 keV M and 1.739 keV K_α energy peaks for cerium and silicon, respectively, are evident. Quantitatively, from the EDS data, the atomic percent ratio of cerium silicon and boron are respectively 0.1:28.4:11.2 Fig. 4(b) shows the excitation and emission spectra of B–SiO_2:Ce^{3+} and pure B–SiO_2 samples. The expectedly observed emission and excitation peaks at 388 nm and 242 nm respectively, are ascribable to the 4f–5d electronic transitions associated with the presence of Ce^{3+} ions [28–30] and the

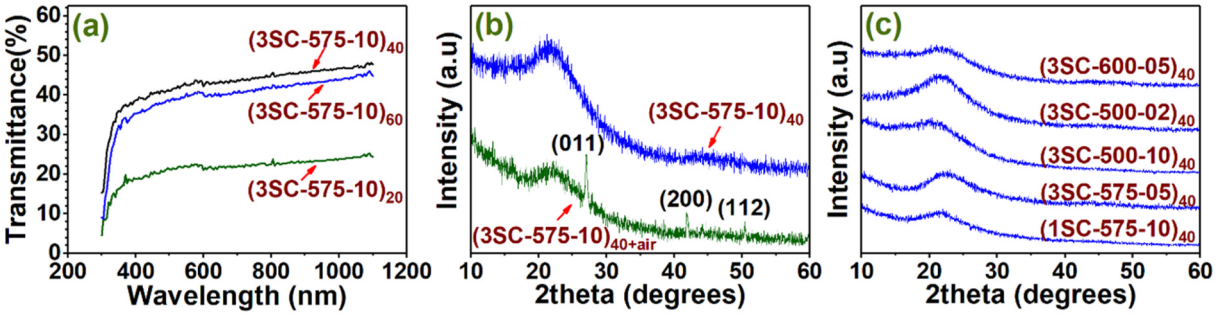

Fig. 3. (a). Optical transmittance spectra of B–SiO_2 densified glass samples with different initial ceramic resin composition. (b) XRD patterns of prepared B–SiO_2 glass samples after densification in air at 700 °C; after densification in vacuum at 700 °C. (c) XRD patterns of prepared B–SiO_2 glass samples under different heat treatments in vacuum indicated in Table 1.

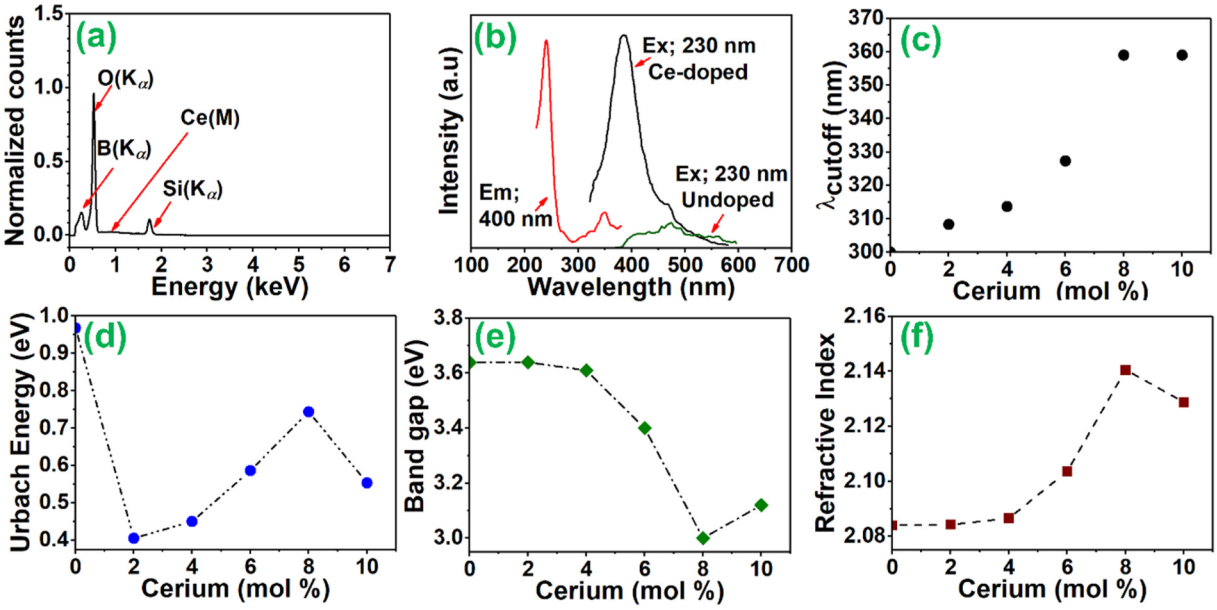

Fig. 4. (a) Energy dispersive spectra of the Ce-doped B–SiO_2 glass (Ce:3SC-575-08)$_{40}$ for a 8 mol % Ce dopant concentration. (b) Photoluminescence excitation (400 nm emission) and emission spectra (230 nm excitation) for undoped and 4 mol % Ce acetate glass. (c–f) The effect of Ce dopant concentration on cut off wavelength, optical band gap, Urbach energy, and refractive index of Ce-doped B–SiO_2 glass, respectively. Broken lines are guides to the eyes only.

deviation of luminescent peak values from other published works is ascribed to the incident radiation interaction with the glass structure as well as effects during the transfer of carriers to the luminescence centers.

The observed luminescence further establishes the capacity of the stereolithographic technique to retain ions in the luminescent trivalent state as against having a competition between the tetravalent states observed during typical melt-quenching in the absence of a reducing atmosphere [28,30–32]. There is no emission in the undoped B–SiO_2 glass at the excitation wavelength considered which indicates the absence of luminescence centers. The optical properties of the Ce-doped glasses were also studied. Fig. S4 gives the reflectance of an arbitrary sample Ce: 3SC-575-08 showing that there is only a 4% reflectance loss for our samples during the transmittance measurements. Fig. 4(c) gives the absorbance cut-off wavelength as a function of increasing cerium concentration. This is the wavelength below which the glass absorbs all of the incident light and it is observed to depend strongly on concentration as expected, ranging from about 300 nm to 360 nm so that there is an overall change of about 60 nm for a concentration change of 10 mol %. This change is comparable to that reported for Ce-doped B–SiO_2 glasses (40 nm for 0.5 wt % Ce_2O_3 change concentration) [33] and increasing trend is similar for other glasses of different compositions [30,33–35]. The increasing trend has been observed in several doped borosilicate glasses [33]. Fig. 4(d–f) show the optical band gap values (E_g), refractive index and Urbach Energy as functions of increasing cerium concentration. The Urbach energy which is characteristic for band edge transition of semiconductors is the width of the tail of localized states corresponding to the optical transition between localized states adjacent to the valence band and the extended states in the conduction band lying above the mobility edge [36]. Lower values for Urbach energy imply the presence of minimal defect (less degree of disorder) and thus a more structurally organized matrix. The presence of these disorders and defects within glass matrix systems typically lead to generation of localized states near or within the conduction band thus increasing band tail widths. Our Urbach energy results show a steep decrease up to 2 mol%, a gradual increase up to 8 mol % and then a decrease up to 10 mol %. In comparison to past reports, for the dopant range of 0–0.5 mol % a similarly decreasing Urbach energy trend is observed in works by Kaur et al. [37] whereas a reverse increasing trend is observed by Lak et al. [38]. Between 0.5 mol % and 1 mol % dopant concentration, a similar decreasing Urbach energy is however observed in both reports [37,38] with increasing cerium dopant concentration. The optical band gap E_g is determined based on the Urbach and Tauc model [8,39] by considering a linear extrapolation to the zero ordinate of a plot of $(ahv^{1/2})$ against the incident photon energy (hv) [40]. The

Tauc plot relation for optical band gap is given by Eq. (1):

$$\frac{h\nu\alpha}{n} = A(h\nu - E_g) \quad (1)$$

where h is the Planck's constant, ν is the vibration frequency, α is the absorption coefficient, E_g is the band gap energy, A is a constant proportionality and n is ½, 3/2, 2 or 3 for a direct, forbidden direct, indirect or forbidden indirect transition respectively. The Urbach energy was estimated based on Eq. (2) by taking the reciprocal slope of a graph of the natural logarithm of the absorption coefficient (lnα) against the incident photon energy (hv) [41].

$$\alpha = \alpha o exp(\frac{h\nu}{Eu}) \quad (2)$$

The refractive index (n) obtained from the optical band gap was determined according to Eq. (3) based on the Lorenz theory:

$$\frac{n^2 - 1}{n^2 + 2} = 1 - \sqrt{(\frac{E_g}{20})} \quad (3)$$

where n is the refractive index and E_g is the optical band gap whereas the reflectance losses were determined based on eqn. (4):

$$R = (\frac{n - 1}{n + 1})^2 \quad (4)$$

The optical band gap is observed to vary from 3.64 to 3.12 for a Cerium dopant concentration range of 0–10% whereas the Urbach energy varies from 0.40 to 0.55 eV. The reflection loss estimated from Eq. (4) and shown in Table 3 show that the scattering losses in this work are comparable to other doped B–SiO_2 by melt quenching ranging between 0.124 and 0.130 in the dopant range we have considered. The observed decrease in band gap and corresponding increase in the Urbach energy with increasing concentration is consistent with the reported band gap changes of 3.53 eV–3.26 eV and Urbach energy changes of 0.61 to 0.25 eV (for 0.5 to 1.5 CeO_2%) [38]. Our result shows a gradual decrease in band gap with increasing dopant concentration which is consistent with reports on cerium doped B–SiO_2 glasses [37,38,42]. This observed change is less steep compared to other reports and band gap values here reported are comparatively higher than similar reports implying less formation of non-bridging oxygen. Non-bridging oxygen binds excited electrons less tightly than bridging oxygen [43]. We ascribe the differences in band gap magnitude at zero cerium dopant concentration compared to the reports in Table 3 to the effects of the other constituents of our borosilicate matrix which expectedly vary from one borosilicate system to the other [37,38,42]. A gradual decrease in optical band gap energy and a corresponding increment in Urbach energy up to 8% Cerium content is observed in our work after which a reverse trend is observed to 10 mol %. This has been ascribed to an increased presence of non-bridging oxygen, increasing concentration of bonding effects and consequent increase of the donor centers within the B–SiO_2 network [8,43,44]. The reverse trend beyond 8% Cerium concentration could be attributed to saturation (a quenching effect) typically observed in doped luminescent systems for some dopant beyond certain doping levels [41]. This effect could be ascribed to an increased interaction between Ce-ion luminescent centers with dopant concentration in the B–SiO_2 matrix as well as non-radiative losses in excitation energies. It should be noted that the determination of bandgap values from the optical absorption has to be performed with care since the scattering could be strong which makes the calculated bandgaps unreasonably smaller than real values (for typical borosilicate glasses). Future studies need to be carried out to compare the bandgap values using other characterization approaches. Fig. 4(f) shows that the refractive index increases from 2.08 to 2.13 for a Ce concentration range of 0%–10%. This increasing trend is consistent with observed increasing values reported for Nd doped glass (2.97–3.026) [45]. In comparison to values obtained for Cerium doped borosilicate glass estimated by the Gladstone Dale relation by Kietly et al. [35], values obtained in this work were about 33% higher than values obtained in their report (~1.5) and this difference is ascribable to be as a result of the difference in borosilicate glass composition. Other previous reports on Cerium doped B–SiO_2 glasses also show a similar increasing refractive index trend with increasing cerium concentration [37]. Again, the quenching effect is also observed beyond 8% Cerium concentration as with the Urbach and band gap energies.

Table 3 further shows the data of other reported values for doped borosilicate glasses with different dopant concentrations. In general, dopant whose oxides have a higher refractive index compared to silica exhibit an increasing refractive index with increasing concentration and the reverse is the case for dopants with oxides whose oxides have a lower refractive index. The theoretically expected refractive index for ideal ceramic composites is given by Eq. (5):

$$\varepsilon = n^2 = \sum v_i n_i^2 \quad (5)$$

where, ε is the dielectric constant, n is the refractive index of the resultant glass, ν_i are the fractional content and n_i are the refractive indices of the individual constituents. Our observed refractive index change is in agreement with equation (4) and the gradient of the refractive index with cerium composition is differs by only 3%.

The reflection loss estimated from eqn (4) and shown in Table 3 show that the scattering losses in this work are comparable to other published works and range between 0.124 and 0.130 in the dopant range we have considered.

Table 3
Summary of some reported optical properties of borosilicate glass with different dopants.

Material composition	Dopant range (%)	Urbach energy change (eV)	Band gap (eV)	Refractive index	Reflection Losses	Method of analysis	Method of sample preparation	Ref.
B–SiO_2:Sm	0.3	[a]1.04	[a]1.01	N/A	N/A	Davis and Mott relation	Melt quenching	[46]
B–SiO_2:Pr	1	[a]1.077	[a]0.942	[a]1.614	0.055	Tauc Relation	Melt quenching	[47]
B–SiO_2:Er	0–4	0.17–0.61	2.56–2.8	2.45–2.53	0.177–0.188	Tauc Relation	Melt quenching	[48]
B–SiO_2:Nd	0.3	[a]1.08	[a]0.96	[a]1.62	0.056	Tauc Relation	Melt quenching	[49]
B–SiO_2:Cr	0–0.8	0.33–0.22	3.79–2.09	N/A	N/A	Tauc Relation	Melt quenching	[50]
B–SiO_2:Mn	0–0.9	0.249–0.275	4.05–3.65	1.65–1.66	0.060–0.062	Tauc Relation	Melt quenching	[51]
B–SiO_2:Co	0–5	0.25–1.2	N/A	N/A	N/A	N/A	Melt quenching	[52]
B–SiO_2:Ti	0–10	0.565–0.48	3.41–3.44	2.61–2.64	0.199–0.203	Tauc Relation	Melt quenching	[53]
B–SiO_2:Pb	0–0.7	0.33–0.37	2.9–2.85	N/A	N/A	Tauc Relation	Melt quenching	[54]
B–SiO_2:Ce	1.8	N/A	[a] 3.37	N/A	N/A	Tauc Relation	Commercial	[54]
B–SiO_2:Ce	0–1	1–0.62	3.15–2.92	2.78–2.85	0.222–0.231	Tauc Relation	Melt quenching	[37]
B–SiO_2:Ce	0–1.5	0.45–0.25	3.53–3.26	1.66–1.68	0.062–0.064	Tauc Relation	Melt quenching	[38]
B–SiO_2:Ce	0–2	N/A	3.00–2.44	N/A	N/A	Tauc Relation	Melt quenching	[42]
B–SiO_2:Ce	2–10	0.4–0.55	3.64–3.12	2.08–2.13	0.124–0.130	Tauc Relation	Stereolithography	This work

[a] Indicates maximum of a reported range of values.

The results of the optical properties for our Cerium doped B–SiO_2 show consistency of the optical properties of luminescent glass fabricated by stereolithography with that of other fabrication processes. The steepness trends also indicate that compared to other reports and methods of fabrication, the stereolithography technique is unique and could accommodate more tunability in a broad dopant concentration while also ensuring uniform doping. Although we have focused on optical properties and characterizations here we intend to further explore higher resolution structures in subsequent works.

4. Conclusion

We have successfully synthesized transparent undoped and Ce doped borosilicate glass with a dopant level of up to 10 mol % by stereolithography calcining and densification in air and vacuum. The calcination temperature is about 98% of the softening temperature and the glass exhibits no devitrification and good optical properties, which can be further modified to yield functional glass materials. Incorporation of Cerium dopants yielded luminescent glass which exhibited a quenching effect at 8% dopant concentration level and a direct band gap. This is, to the best of our knowledge, one of the first reports on the fabrication of amorphous borosilicate glass via stereolithography. Our fabrication approach provides a potentially promising path for the application of vat photopolymerization, powder bed fusion and other additive manufacturing techniques for B–SiO_2 glass fabrication. It is a procedure that will allow for rapid, digital and on-demand manufacturing for advanced optical and luminescence systems.

Declaration of competing interest

The authors declare that there is no known competing financial interests or personal relationships that could have appeared to influence work published herein.

Acknowledgments

The authors would like to thank (i) Advanced Materials Engineering Research Institute (AMERI, FIU) (ii) Center for Study of Matter at Extreme Conditions (CESMEC, FIU) for the use of their facilities. C.Wang and N.Pala also acknowledge financial support from National Science Foundation (OISE #2107318). We also acknowledge the Florida International University Dissertation Year Fellowship.

Appendix A. Supplementary data

Supplementary data to this article can be found online at https://doi.org/10.1016/j.ceramint.2022.01.141.

References

[1] C. Canevali, M. Mattoni, F. Morazzoni, R. Scotti, M. Casu, A. Musinu, R. Krsmanovic, S. Polizzi, A. Speghini, M. Bettinelli, Stability of luminescent trivalent cerium in silica host glasses modified by boron and phosphorus, J. Am. Chem. Soc. (2005) 14681–14691, https://doi.org/10.1021/ja052502o.

[2] K.S. Rudramamba, S.K. Taherunnisa, M. Rami Reddy, The role of CuO as limiting and luminescent probe for orange red emission of Sm3+ ions in strontium bismuth borosilicate glasses, Opt. Mater. (2020), https://doi.org/10.1016/j.optmat.2020.110340.

[3] Z. Tang, Z. Huang, W. Han, J. Qi, N. Ma, Y. Zhang, T. Lu, Microwave-assisted synthesis of uranium doped Y2Zr2O7 transparent ceramics as potential near-infrared optical lens, Scripta Mater. (2020) 90–93, https://doi.org/10.1016/j.scriptamat.2019.11.007.

[4] M.H. Jo, B.R. Koo, H.J. Ahn, Fe co-doping effect on fluorine-doped tin oxide transparent conducting films accelerating electrochromic switching performance, Ceram. Int. (2020) 10578–10584, https://doi.org/10.1016/j.ceramint.2020.01.061.

[5] Z. Wang, L. Gan, W. Huang, Structural recovery and optical properties stabilization of CeO2/TiO2-doped boroaluminosilicate glass under gamma irradiation, Radiat. Phys. Chem. (2018) 133–140, https://doi.org/10.1016/j.radphyschem.2018.05.033.

[6] J. An, Z. Zhang, Y. Qiu, Z.Y. Fu, Y. Zhou, F. Zeng, Luminescence properties of borosilicate glass doped with Ce3+/Dy3+/Eu3+ under ultraviolet excitation for white LED, J. Non-Cryst. Solids (2019) 208–213, https://doi.org/10.1016/j.jnoncrysol.2018.09.050.

[7] X.Y. Sun, Z.H. Xiao, Y.T. Wu, X.G. Yu, Q.L. Hu, Y. Yuan, Q. Liu, C. Struebing, Z. Kang, Role of Al3+ on tuning optical properties of Ce3+-activated borosilicate scintillating glasses prepared in air, J. Am. Ceram. Soc. (2018) 4480–4485, https://doi.org/10.1111/jace.15773.

[8] A. Saeed, Y.H. Elbashar, S.U. El Kameesy, Optical spectroscopic analysis of high density lead borosilicate glasses, Silicon (2018) 185–189, https://doi.org/10.1007/s12633-015-9391-7.

[9] H.A. Elbatal, A.M. Abdelghany, F.H. Elbatal, F.M. Ezzeldin, Gamma rays interactions with WO 3-doped lead borate glasses, Mater. Chem. Phys. (2012) 542–548, https://doi.org/10.1016/j.matchemphys.2012.03.032.

[10] B. Seyfarth, G. Matthäus, T. Ullsperger, S. Nolte, L. Schade, A. Tunnermann, in: Selective Laser Melting of Glass Using Ultrashort Laser Pulses, 2018, https://doi.org/10.1117/12.2289614.

[11] F. Klocke, A. McClung, C. Ader, Direct laser Sintering of Borosilicate glass, Proc. Solid Freeform Fabrication Symp. (2004) 214–219.

[12] J. Luo, J.T. Goldstein, A.M. Urbas, D.A. Bristow, R.G. Landers, E.C. Kinzel, in: Additive Manufacturing of Borosilicate Glass, SPIE-Intl Soc Optical Eng, 2017, p. 8.

[13] J. Luo, T. Bender, D.A. Bristow, R.G. Landers, J.T. Goldstein, A.M. Urbas, E. C. Kinzel, Bubble Formation in Additive Manufacturing of Borosilicate Glass, Proc. Solid Freeform Fabrication Symp., 2016, pp. 998–1003.

[14] J. Klein, M. Stern, G. Franchin, M. Kayser, C. Inamura, S. Dave, J.C. Weaver, P. Houk, P. Colombo, M. Yang, N. Oxman, Additive manufacturing of optically transparent glass, 3D print, Addit. Manuf. (2015) 92, https://doi.org/10.1089/3dp.2015.0021.

[15] F. Kotz, K. Arnold, W. Bauer, D. Schild, N. Keller, K. Sachsenheimer, T.M. Nargang, C. Richter, D. Helmer, B.E. Rapp, Three-dimensional printing of transparent fused silica glass, Nature 544 (2017) 337, https://doi.org/10.1038/nature22061.

[16] I. Cooperstein, E. Shukrun, O. Press, A. Kamyshny, S. Magdassi, Additive manufacturing of transparent silica glass from solutions, ACS Appl. Mater. Interfaces 10 (2018) 18879–18885, https://doi.org/10.1021/acsami.8b03766.

[17] D.T. Nguyen, C. Meyers, T.D. Yee, N.A. Dudukovic, J.F. Destino, C. Zhu, E.B. Duoss, T.F. Baumann, T. Suratwala, J.E. Smay, R. Dylla-Spears, 3D printing: 3D-printed transparent glass, Adv. Mater. 26/2017), Adv. Mater. 29 (2017) 1701181, https://doi.org/10.1002/adma.201770191.

[18] T. Moritz, J. Schilm, A. Rost, E. Schwarzer, S. Weingarten, U. Scheithauer, K. Wätzig, D. Wagner, A. Michaelis, Ceramic additive manufacturing methods applied to sintered glass components with novel properties, Ceram. Mod. Technol. 1 (2019) 111–119, https://doi.org/10.29272/CMT.2019.0008.

[19] J. Cesarano III, P.D. Calvert, Freeforming objects with low-binder slurry. US6027326A, 2000.

[20] G.M. Gratson, F. García-Santamaría, V. Lousse, M. Xu, S. Fan, J.A. Lewis, P. V. Braun, Direct-write assembly of three-dimensional photonic crystals: conversion of polymer scaffolds to silicon hollow-woodpile structures, Adv. Mater. 18 (2006) 461–465, https://doi.org/10.1002/adma.200501447.

[21] C.M. Larson, J.J. Choi, P.A. Gallardo, S.W. Henderson, M.D. Niemack, G. Rajagopalan, R.F. Shepherd, Direct ink writing of silicon carbide for microwave optics, Adv. Eng. Mater. 18 (2016) 39–45, https://doi.org/10.1002/adem.201500298.

[22] K. Sun, T.S. Wei, B.Y. Ahn, J.Y. Seo, S.J. Dillon, J.A. Lewis, 3D printing of interdigitated Li-ion microbattery architectures, Adv. Mater. 25 (2013) 4539–4543, https://doi.org/10.1002/adma.201301036.

[23] C.W. Hull, C.W. Lewis, Method of and Apparatus for Production of Three Dimensional Objects by Stereolithography. US4999143A, 1992.

[24] B. Rapp, F. Kotz, Composition and method for producing a shaped body from high-purity, transparent quartz glass by means of additive manufacturing. DE102016012003A1, 2017.

[25] O. Omena, P. Nezih, W. Chunlei, Glass Scintillators and Methods of Manufacturing the Same - US10940639B1, 2021.

[26] P. Norby, Synchrotron powder diffraction using imaging plates: crystal structure determination and rietveld refinement, J. Appl. Crystallogr. (1997) 21–30, https://doi.org/10.1107/S0021889896009995.

[27] S. Thakral, M.W. Terban, N.K. Thakral, R. Suryanarayanan, Recent advances in the characterization of amorphous pharmaceuticals by X-ray diffractometry, Adv. Drug Deliv. Rev. (2016) 183–193, https://doi.org/10.1016/j.addr.2015.12.013.

[28] Y. Isokawa, D. Nakauchi, G. Okada, N. Kawaguchi, T. Yanagida, Radiation induced luminescence properties of Ce-doped Y2O3-Al2O3-SiO2 glass prepared using floating zone furnace, J. Alloys Compd. (2019) 859–864, https://doi.org/10.1016/j.jallcom.2018.12.245.

[29] W. Chewpraditkul, Y. Shen, D. Chen, B. Yu, P. Prusa, M. Nikl, A. Beitlerova, C. Wanarak, Luminescence and scintillation of Ce3+-doped high silica glass, Opt. Mater. (2012) 1762–1766, https://doi.org/10.1016/j.optmat.2012.04.012.

[30] Y. Tratsiak, M. Korzhik, A. Fedorov, G. Dosovitsky, O. Akimova, S. Belus, M. Fasoli, A. Vedda, V. Mechinsky, E. Trusova, On the stabilization of Ce, Tb, and Eu ions with different oxidation states in silica-based glasses, J. Alloys Compd. (2019) 302–308, https://doi.org/10.1016/j.jallcom.2019.05.105.

[31] K. Kagami, Y. Fujimoto, M. Koshimizu, D. Nakauchi, T. Yanagida, K. Asai, Photoluminescence and radiation response properties of CsPO3-Al(PO3)3-CeCl3-based glass scintillators, Opt. Mater. (2019) 127–131, https://doi.org/10.1016/j.optmat.2018.04.036.

[32] H. El Hamzaoui, B. Capoen, N. Al Helou, G. Bouwmans, Y. Ouerdane, A. Boukenter, S. Girard, C. Marcandella, O. Duhamel, G. Chadeyron, R. Mahiou, M. Bouazaoui, Cerium-activated sol-gel silica glasses for radiation dosimetry in harsh

environment, Mater. Res. Express (2016) 046201, https://doi.org/10.1088/2053-1591/3/4/046201.
[33] C. Jiang, Q. Zeng, F. Gan, Scintillation luminescence of cerium-doped borosilicate glass containing rare-earth oxide, Hard X-Ray, Gamma-Ray, Neutron Detect, Phys. II. 4141 (2000) 316–323, https://doi.org/10.1117/12.407593.
[34] L. Dong, A.K. Agarwal, D.J. Beebe, H. Jiang, Adaptive liquid microlenses activated by stimuli-responsive hydrogels, Nature 442 (2006) 551–554, https://doi.org/10.1038/nature05024.
[35] M.W. Kielty, M. Dettmann, V. Herrig, M.G. Chapman, M.R. Marchewka, A. A. Trofimov, U. Akgun, L.G. Jacobsohn, Investigation of Ce3 + luminescence in borate-rich borosilicate glasses, J. Non-Cryst. Solids 471 (2017) 357–361, https://doi.org/10.1016/J.JNONCRYSOL.2017.06.022.
[36] N. Ghobadi, Band gap determination using absorption spectrum fitting procedure, Int. Nano Lett. (2013) 1–4, https://doi.org/10.1186/2228-5326-3-2.
[37] R. Kaur, R.B. Rakesh, S.G. Mhatre, V. Bhatia, D. Kumar, H. Singh, S.P. Singh, A. Kumar, Thermoluminescence, structural and optical properties of Ce3+ doped borosilicate doped glasses, J. Mater. Sci. Mater. Electron. 3213 (32) (2021) 18381–18396, https://doi.org/10.1007/S10854-021-06382-8, 2021.
[38] F. Lak, M. Rezvani, Optical characterization of BK7 borosilicate glasses containing different amounts of CeO2, Adv. Ceram. Prog. 2 (2016) 17–24, https://doi.org/10.30501/ACP.2016.70026.
[39] J. Tauc, A. Menth, States in the gap, J. Non-Cryst. Solids 8–10 (1972) 569–585, https://doi.org/10.1016/0022-3093(72)90194-9.
[40] P. Limkitjaroenporn, J. Kaewkhao, P. Limsuwan, W. Chewpraditkul, Physical, optical, structural and gamma-ray shielding properties of lead sodium borate glasses, J. Phys. Chem. Solid. (2011) 245–251, https://doi.org/10.1016/j.jpcs.2011.01.007.
[41] S. Insitipong, J. Kaewkhao, T. Ratana, P. Limsuwan, Optical and structural investigation of bismuth borate glasses doped with Dy3+, Procedia Eng. 8 (2011) 195–199, https://doi.org/10.1016/j.proeng.2011.03.036.
[42] P. Kaur, G.P. Singh, S. Kaur, D.P. Singh, Modifier role of cerium in lithium aluminium borate glasses, J. Mol. Struct. 1020 (2012) 83–87, https://doi.org/10.1016/J.MOLSTRUC.2012.03.053.
[43] A. Bahadur, Y. Dwivedi, S.B. Rai, Optical properties of cerium doped oxyfluoroborate glass, Spectrochim. Acta Part A Mol. Biomol. Spectrosc. (2013) 400–403, https://doi.org/10.1016/j.saa.2013.03.066.
[44] Z. Hussain, Optical band gap, oxidation polarizability, optical basicity and electronegativity measurements of silicate glasses using ellipsometer and abbe refractometer, New J. Glass Ceram. 11 (2021) 1–33, https://doi.org/10.4236/njgc.2021.111001.
[45] R. Kaur, R.B. Rakesh, S.G. Mhatre, V. Bhatia, D. Kumar, H. Singh, S.P. Singh, A. Kumar, Physical, optical, structural and thermoluminescence behaviour of borosilicate glasses doped with trivalent neodymium ions, Opt. Mater. 117 (2021), 111109, https://doi.org/10.1016/j.optmat.2021.111109.
[46] P. Goyal, Y.K. Sharma, S. Pal, U.C. Bind, S.C. Huang, S.L. Chung, Structural, optical and physical analysis of B2O3–SiO2–Na2O–PbO–ZnO glass with Sm3+ ions for reddish–orange laser emission, J. Lumin. 192 (2017) 1227–1234, https://doi.org/10.1016/J.JLUMIN.2017.08.061.
[47] S.P. Priyanka Goyal, , U.C.B., Y.K. Sharma, Structural and physical analysis of borosilicate glasses with Pr3+ ions, Adv. Mater. Process. 2 (2017) 119–124.
[48] N.A.N. Razali, I.S. Mustafa, N.Z.N. Azman, H.M. Kamari, A.A. Rahman, K. Rosli, N. S. Taib, N.A. Tajuddin, The physical and optical studies of erbium doped borosilicate glass, J. Phys. Conf. Ser. 1083 (2018), 012004, https://doi.org/10.1088/1742-6596/1083/1/012004.
[49] Yogesh Kumar Sharma, Priyanka Goyal, Sudha Pal, Umesh Chandra Bind, Optical and physical analysis of Nd3+ doped borosilicate glasses, J. Mater. Sci. Eng. B. 5 (2015) 406–417, https://doi.org/10.17265/2161-6221/2015.11-12.002.
[50] E. Ebrahimi, M. Rezvani, Optical and structural investigation on sodium borosilicate glasses doped with Cr2O3, Spectrochim. Acta Part A Mol. Biomol. Spectrosc. 190 (2018) 534–538, https://doi.org/10.1016/J.SAA.2017.09.031.
[51] M.Y. Hassaan, H.M. Osman, H.H. Hassan, A.S. El-Deeb, M.A. Helal, Optical and electrical studies of borosilicate glass containing vanadium and cobalt ions for smart windows applications, Ceram. Int. 2 (2017) 1795–1801, https://doi.org/10.1016/J.CERAMINT.2016.10.137.
[52] K.S. Shaaban, I. Boukhris, I. Kebaili, M.S. Al-Buriahi, Spectroscopic and attenuation shielding studies on B2O3-SiO2-LiF- ZnO-TiO2 glasses, Silicon (2021) 1–10, https://doi.org/10.1007/S12633-021-01080-W, 2021.
[53] C.R. Gautam, S. Das, S.S. Gautam, A. Madheshiya, A.K. Singh, Processing and optical characterization of lead calcium titanate borosilicate glass doped with germanium, J. Phys. Chem. Solid. 115 (2018) 180–186, https://doi.org/10.1016/J.JPCS.2017.12.038.
[54] S. Baccaro, A. Cemmi, I. Di Sarcina, F. Menchini, Gamma rays effects on the optical properties of cerium-doped glasses, Int. J. Appl. Glass Sci. 6 (2015) 295–301, https://doi.org/10.1111/IJAG.12131.